Effect of nanoscale phase separation on the fracture behavior of glasses: Toward tough, yet transparent glasses

Longwen Tang, N. M. Anoop Krishnan, Jonathan Berjikian, Jared Rivera, Morten M. Smedskjaer, John C. Mauro, Wei Zhou, and Mathieu Bauchy

Phys. Rev. Materials **2**, 113602 — Published 8 November 2018

DOI: 10.1103/PhysRevMaterials.2.113602

Effect of nanoscale phase separation on the fracture behavior of glasses: Toward tough, yet transparent glasses

Longwen Tang[a,b], N. M. Anoop Krishnan[b,c], Jonathan Berjikian[b], Jared Rivera[b], Morten M. Smedskjaer[d], John C. Mauro[e], Wei Zhou[a,*], Mathieu Bauchy[b,*]

a *State Key Laboratory of Water Resources and Hydropower Engineering Science, Wuhan University, Wuhan 430072, China*

b *Physics of AmoRphous and Inorganic Solids Laboratory (PARISlab), Department of Civil and Environmental Engineering, University of California, Los Angeles, CA 90095, USA*

c *Department of Civil Engineering, Indian Institute of Technology Delhi, Hauz Khas, New Delhi 110016, India*

d *Department of Chemistry and Bioscience, Aalborg University, 9220 Aalborg, Denmark*

e *Department of Materials Science and Engineering, The Pennsylvania State University, University Park, PA 16802, USA*

Although oxide glasses have many unique properties, their range of applications remains limited by their brittleness. By mimicking the microstructure of composite materials, the presence of controlled nanoscale phase separation in glass could overcome this limitation. However, the nature of the toughening mechanism induced by such nanostructuring remains poorly understood. Here, based on peridynamic simulations, we investigate the effect of nanoscale

phase separation on the crack propagation mechanism. We show that phase separation can significantly increase glass' toughness (with up to a 90% increase in the fracture energy for the range of conditions investigated herein). The extent of toughening is found to arise from a balance between the overall cohesion of the phase-separated glass and the propensity for crack deflection. This suggests that controlled nanoscale phase separation is a promising route toward the development of tough, yet optically transparent glasses.

Keywords: Phase separation, glass, peridynamics, crack deflection, toughening mechanism

I. INTRODUCTION

Thanks to their unique optical, chemical, and mechanical properties, glasses have been key enablers for modern human civilization (e.g., windows, lenses, containers, etc.) [1]. This societal impact has only increased as the use of glasses for liquid crystal display panels, optical fibers, and damage-resistant protective covers has transformed the way in which humans interact with computing devices and with each other [2]. However, despite recent advances in the mechanical performance of glass [3], it still achieves only a fraction of its theoretical strength and remains mechanically brittle. In contrast to crystals, glasses lack a stable shearing mechanism and, hence, show very poor ductility and high brittleness [4]. As such, the fracture toughness (K_{Ic}, the resistance to fracture) of most inorganic, non-metallic glasses remains between 0.2-1.4 $MPa{\cdot}m^{1/2}$ [5].

The brittleness of glass is the main limitation of its use in many applications, since impacts, scratching, or fatigue can result in undesirable or even dangerous fracture [2,3]. This is a serious safety concern, as the number of injuries related to glass breakage (e.g., during car crashes) is

significant. Furthermore, improving the mechanical properties of glasses is crucial to address major challenges in energy, communications, and infrastructure—brittleness is a major bottleneck for further development in short-haul high-capacity telecommunication, fiber-to-the-home technologies, flexible substrates and roll-to-roll processing of displays, solar modules, planar lighting devices, next-generation touch-screen devices, large scale and high altitude architectural glazing, etc [3]. Increasing the strength and fracture toughness of glass would also lead to a significant reduction of material investment and energy and production costs for existing applications while achieving comparable or improved performance. Among other applications, this could enable the design of tough, yet light car windshields that would reduce fuel consumption.

Much effort has been made to enhance the toughness of glass by means of intrinsic and extrinsic toughening strategies [5,6]. On the one hand, extrinsic techniques rely on the use of reinforcements to control the driving force behind the crack tip, e.g., through crack-tip shielding or crack-bridging [6–9]. However, such reinforcements usually significantly hinder the transparency of glass [3]. On the other hand, intrinsic techniques rely on the optimization of the inherent fracture resistance of the matrix by tuning their atomic structure or microstructure—with some partial success [10,11].

As an alternative route, phase separation—which arises from liquid–liquid immiscibility in the melt [12,13]— has been suggested to potentially enhance the fracture toughness of glasses [14–17]. Depending on the glass composition, phase separation can occur via (i) a nucleation-growth mechanism, which results in the formation of spherical droplets within a glassy matrix or (ii) spinodal decomposition, which yields two interconnected glassy phases [18]. By inducing the appearance of a microstructure within an initially homogeneous material, phase separation

mimics the toughening strategy that has been successfully used in composite materials [7,9,19–25]. Indeed, the insertion of particles in brittle phases has been shown to induce various toughening mechanisms, including crack deflection [26,27], trapping [28–30], pinning [31] or bridging [32,33]. Although the formation of large phases (with droplets larger 500 nm or resulting from spinodal decomposition) typically induces a loss of transparency in the glass [34], it has recently been shown that the dimensions of the droplets forming upon phase separation in calcium aluminosilicate glasses can be finely controlled (from 20 to 500 nm) [35], which makes it possible for phase-separated glasses to retain their transparency in the visible spectrum. However, the toughening mechanism of such nanoscale phase separation in glasses remains unknown.

Here, we investigate the effect of nanoscale phase separation on the fracture behavior of glass using peridynamic simulations. We demonstrate that nanoscale phase separation can significantly increase the fracture toughness of glasses (by up to 90% based on the range of parameters explored here). The increase in the fracture toughness is found to be controlled by a competition between the overall cohesion of the phase separated glass and the propensity for crack deflection at the droplet-matrix interfaces. This suggests that, when properly controlled and optimized, phase separation can yield tough, yet optically transparent glasses.

II. METHODS

A. Peridynamic theory

Although many studies have focused on investigating the fracture of composite materials, they typically rely on the finite element method (FEM), which, in turn, relies on a differential formulation of mechanics (i.e., based on partial differential equations) [43,44]. As such, this approach may yield unrealistic results—due to numerical difficulties arising from the existence

of discontinuities within the simulated system, e.g., stress discontinuities during crack propagation or in composite materials [40], which are not well handled by methods relying on partial differential equations. In turn, the peridynamic method is based on a non-local formulation of mechanics [36–38]. Rather than relying on partial differential equations (as usually considered in FEM [39]), the peridynamic formalism involves integral equations. This integral formulation allows one to avoid the numerical difficulties arising from the use of FEM in composite materials and makes peridynamics an attractive method to simulate crack propagation.

In peridynamics, the material domain is discretized into points with a finite volume. Each material point **x** interacts with the other points **x'** that are located within a specific region $\mathcal{H}$x, which is called the family of **x**. For convenience, this region is often assumed to be a sphere centered around **x** with a radius δ, which is known as the horizon. The relative position between two interacting points is defined as a bond $\boldsymbol{\xi}$, which can be expressed as:

$$\boldsymbol{\xi} = \mathbf{x} - \mathbf{x}' \tag{1}$$

The relative displacement between two points is defined as $\boldsymbol{\eta}$ and can be expressed as:

$$\boldsymbol{\eta} = \mathbf{u}(\mathbf{x}', t) - \mathbf{u}(\mathbf{x}, t) \tag{2}$$

where **u** is the displacement vector field. Within the peridynamic formalism, the equation of motion , based on the conservation of linear momentum, can then be expressed as:

$$\rho(\mathbf{x})\ddot{\mathbf{u}}(\mathbf{x}, t) = \int_{\mathcal{H}x} \left\{ \underline{\mathbf{T}}[\mathbf{x}, t]\langle \mathbf{x}' - \mathbf{x} \rangle - \underline{\mathbf{T}}[\mathbf{x}', t]\langle \mathbf{x} - \mathbf{x}' \rangle \right\} dV_{\mathbf{x}'} + \mathbf{b}(\mathbf{x}, t) \tag{3}$$

where t is the time, ρ is the local density, **b**(**x**, t) is the external body force density, $dV_{x'}$ is an infinitesimal volume around **x'**, and $\underline{\mathbf{T}}$ is called the force vector state that describes the

interaction force between points. Note that $\underline{\mathbf{T}}$ depends on the constitutive model used in the peridynamics simulation, e.g., linear elastic, elasto-plastic etc., governing the mechanical response of the material. For the ordinary state-based model, the constitutive model can be expressed as:

$$\underline{\mathbf{T}} = \begin{cases} \underline{C}\dfrac{\boldsymbol{\xi}+\boldsymbol{\eta}}{\|\boldsymbol{\xi}+\boldsymbol{\eta}\|} & \|\boldsymbol{\xi}+\boldsymbol{\eta}\| \neq 0 \\ 0 & \|\boldsymbol{\xi}+\boldsymbol{\eta}\| = 0 \end{cases} \tag{4}$$

where $\underline{C}$ is the scalar state, which is determined by the elastic parameters of material.

In this study, we adopt the linear peridynamics solid (LPS) constitutive model introduced by Silling [41], which assumes that the force is proportional to the deformation following the linear elastic response until the fracture point is reached. The scalar state is then given by:

$$\underline{C} = \frac{3K\theta}{m}\underline{\omega x} + \frac{15G}{m}\underline{\omega e}^{d} \tag{5}$$

where $\underline{\omega}$ is an influence function, m is a weighted volume, $\underline{e}^{d}$ is the deviatoric part the extension scalar state $\underline{e}$, θ is the dilatation (a measure of the volumetric strain at small deformation), and K and G are the bulk and shear moduli, respectively.

In peridynamics, the formation and propagation of cracks are modeled via the breaking the bonds, $\boldsymbol{\xi}$, that initially exist between each material points and its family. A given bond is considered broken if the bond stretching $\boldsymbol{\eta}$ exceeds a threshold value s_c, which depends on the constitutive model. At this point, the interaction between these points cease to exist. For three-dimensional systems, s_c can be determined as [42]:

$$S_c = \sqrt{\frac{G_c}{\left(3G + (\frac{3}{4})^4 \left(K - \frac{5G}{3}\right)\right)\delta}} \tag{6}$$

where G_c is the fracture energy of the material.

B. Generation of the phase-separated microstructures

To assess the effect of nanoscale phase separation on the mechanical response of glasses, two initial configurations are considered: (i) a homogeneous glass (see Fig. 1(a)) and (ii) a phase-separated glass containing some spherical nanoinclusions (see Fig. 1(b)). Note that, here, we do not attempt to simulate the type of microstructure that would result from spinodal decomposition as such microstructure would likely compromise glass transparency. The nanoinclusion diameter is fixed at 200 nm, which is small enough for the glass to retain its transparency [35]. Both systems have a cubic geometry, free surface boundary conditions, and comprise an initial notch of 200 nm to induce some stress concentration and initiate the crack in the middle plane. In addition, a series of simulations using systems of varying lengths L (from 500 nm to 3000 nm) are performed to investigate the influence of the system size. We find that the computed fracture energy shows a fair convergence for L >1000 nm. This is consistent with previous results suggesting that, for composite materials, the simulated system should at least 5 times larger than the diameter of the inclusions [43,44]. In the following, the length of the system is chosen to be constant and equal to 1000 nm. In the case of the phase-separated glass, the nanoinclusions are initially placed within the glass via the taking-placing procedure [45], by randomly inserting a given number of spheres within the cubic matrix while ensuring the absence of any overlap. The number of nanoinclusions is fixed so that their volume fraction is 30%—a realistic value based on experimental observations [35].

The peridynamic domain is then discretized into lattice points with a simple cubic lattice structure of constant grid spacing. Previous studies suggested that peridynamic models can properly describe the fracture behavior of composite systems when the grid spacing is equal to or smaller than a tenth of the particle diameter [46,47]. In this study, a grid spacing of 16.7 nm is found to yield a convergence of the computed stress-strain curve. The horizon is defined as three times the grid spacing. The mechanical properties of each point are then assigned based on the phase it belongs to (i.e., matrix or nanoinclusion). The Young's modulus E^{mat} and fracture energy G_c^{mat} of the glass matrix are fixed as 93 GPa and 4.5 J/m^2, i.e., to mimic the mechanical properties of a calcium aluminosilicate glass [48]. The effect of the stiffness and toughness of the nanoinclusions is then investigated by considering varying values of nanoinclusion Young's modulus E^{part} (from $0.5E^{mat}$ to $2E^{mat}$) and fracture energy G_c^{part} (from $0.5G_c^{mat}$ to $2.5G_c^{mat}$). Note that, in practice, the phase separation of calcium aluminosilicate glasses can result in the formation of stiff/weak or soft/tough nanoinclusions consisting of Ca- or Si-rich droplets, respectively [35]. The Poisson's ratios of all phases are fixed as 0.3. These inputs are used to define the constitutive model of each phase (see Eqs. 4 and 5). Based in the fact that experiments suggest the existence of a strong interface between the nanoinclusions and matrix (which arises from strong Van der Waals forces) [35], the constitutive model governing the bonds across the interface are here assumed to be the same as those of the matrix.

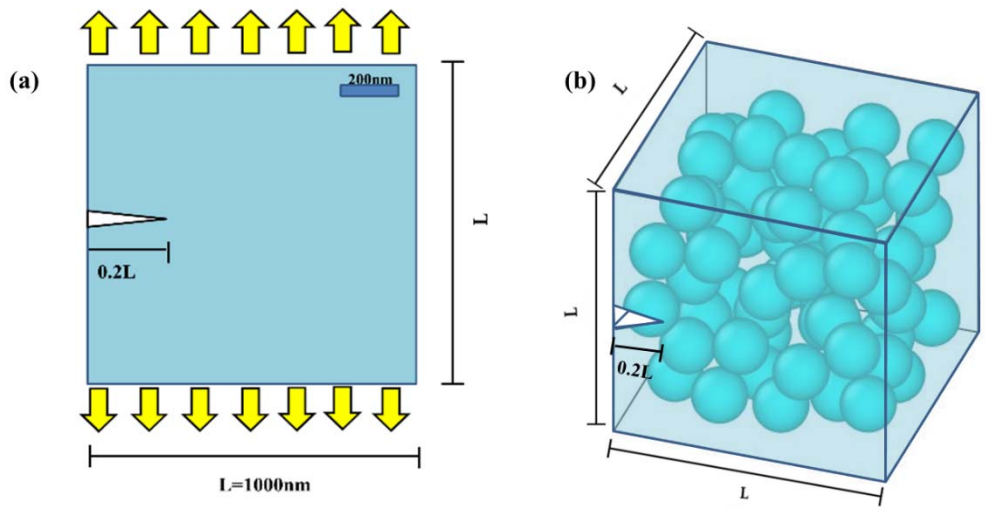

Figure 1. Schematic describing the geometry of a (a) homogeneous and (b) "droplet phase-separated" glass subjected to uniaxial tension.

C. Simulations of mode I fracture

The mode I fracture of the phase-separated glasses is then investigated by subjecting each configuration to a displacement-controlled tensile load. This is achieved by assigning some constant velocities to the top and bottom boundaries of the sample. A boundary thickness of 3 grid spacings is used to avoid any spurious effect arising from non-local interactions close to the free surface [42]. To ensure the stability of the simulation, the integration timestep is selected based on a von Neumann stability analysis [37]. The simulations are performed by using the open-source Peridigm package [49]. The fracture energy of the phase-separated glasses is obtained by integrating the stress-strain curve as follows:

$$G_c^{glass} = s_0 \int \sigma_z dl_z \tag{7}$$

where σ_z and l_z are the stress and displacement in the loading direction (z-axis), respectively. The term s_0 is a unitless correction factor (equal to 1.25 herein) that accounts for the existence of the initial notch in the glass.

III. RESULTS AND DISCUSSION

A. Effect of the strain rate

We first assess the effect of the strain rate on the fracture behavior of phase-separated glasses. Fig. 2 shows the computed stress-strain curve and fracture energy for select strain rates for a phase-separated glass with E^{part} = 72.5 GPa, E^{mat} = 93 GPa, G_c^{mat} = 9.2 J/m^2, and G_c^{part} = 4.5 J/m^2. Overall, we observe that the system exhibits a fairly elastic response, wherein stress linearly increases with strain until the fracture point is reached (see Fig. 2(a)). We note that the elastic regime remains unaffected by the strain rate. However, at high strain rate (> 10^6 s^{-1}), we observe the appearance of some ductility, which manifests itself as an increase in the fracture energy of the system (see Fig. 2(b)). This can be explained by the fact that, when the strain rate increases, inertia effects around the crack tip becomes noticeable, which can result in crack branching or zig-zag crack path [50]. In turn, we observe that both the stress–strain curve and resulting fracture energy converge when the strain rate becomes lower than of 10^5 s^{-1}. This suggests that, although such strain rate remains high as compared to those achieved experimentally, the fracture response of phase-separated glasses only weakly depends on the strain rate in this regime. This likely arises from the fact that the simulated system is relatively small so that the inertia effects can be neglected for this range of strain rates. Note that, the same convergence can also be observed when the mechanical properties are varied (for the range of values considered herein). In the following, for the sake of balance between computational efficiency and accuracy, we keep a fixed strain rate of 8×10^4 s^{-1}.

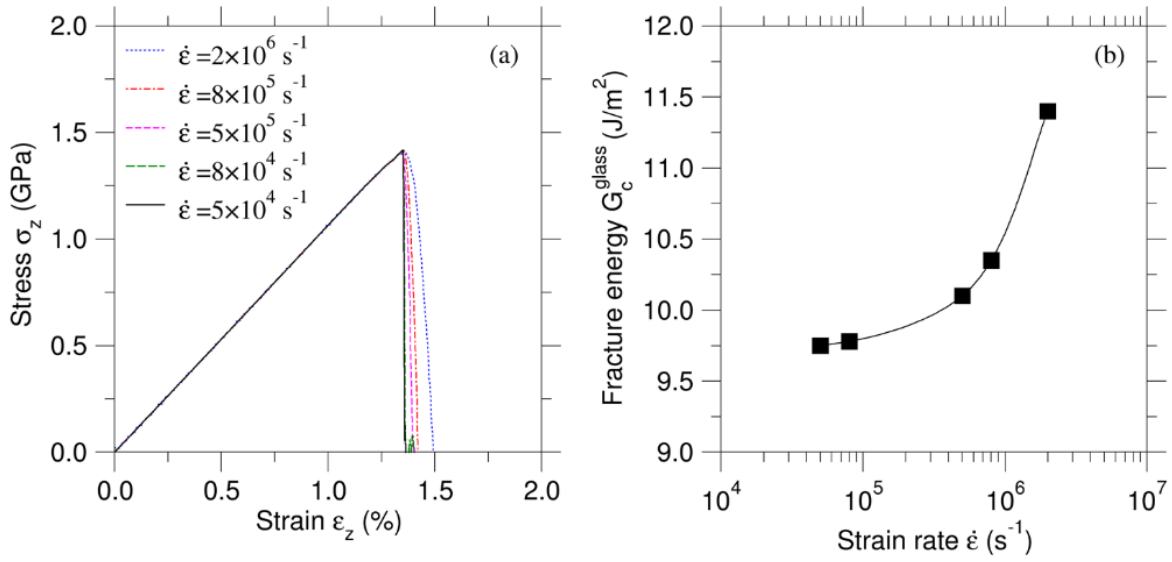

Figure 2. Computed (a) stress–strain curve and (b) fracture energy of the phase-separted glass under different strain rates. The solid line in panel (b) is shown to guide the eye.

B. Effect of the stiffness of the nanoinclusions

We now assess the effect of a dissimilarity in stiffness between the matrix and nanoinclusions. Fig. 3(a) shows the stress-strain curves of phase-separated glasses for selected Young's modulus values for the nanoinclusions while keeping their fracture energy fixed. As expected, we observe that the overall stiffness (i.e., the slope of the stress–strain curve) of the phase-separated glasses increases with increasing Young's modulus of the nanoinclusions. However, the presence of softer inclusions results in an increase in the ultimate strain before fracture. This arises from the fact that soft particles locally reduce the stress experienced by the glass and, thereby, postpone the yielding of the system.

Fig. 3(b) shows the evolution of the resulting fracture energy of the phase-separated glasses as a function of the Young's modulus of the nanoinclusions (for selected nanoinclusion fracture

energies). At fixed fracture energy for each phase, we observe that the fracture energy of the phase-separated glass is minimum when the stiffness of the matrix and nanoinclusions is similar. In turn, the fracture energy of the system increases as the nanoinclusions become softer or stiffer than the glass matrix. This minimum results from the competition between the two effects previously mentioned, that is, the variations in the stiffness and ultimate strain of the phase-separated glass. However, we note that the effect of a dissimilarity of stiffness between the matrix and nanoinclusions is not symmetric. In particular, the increase in the fracture energy is found to be more pronounced (i) for stiffer nanoinclusions when those are weaker than the matrix (i.e., with lower fracture energy) and (ii) for softer nanoinclusions when those are tougher than the matrix. The origin of these distinct effects will be discussed in Sec. 3.4.

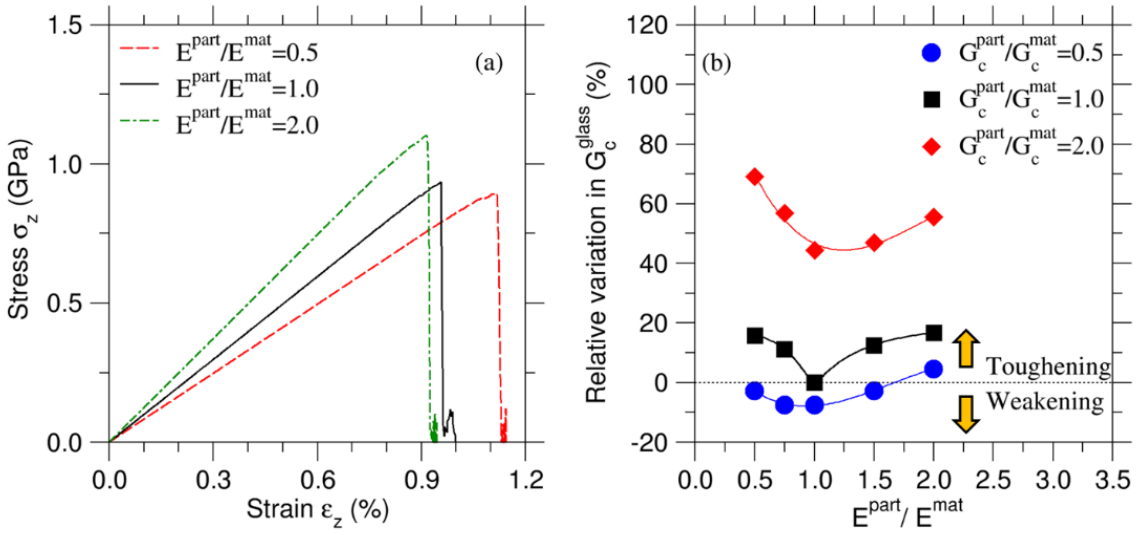

Figure 3. (a) Computed stress–strain curves for selected values of Young's modulus (E^{part}) for the nanoinclusion particles—the properties of the matrix (E^{mat}, G_c^{mat}) remaining constant and with $G_c^{part} = G_c^{mat}$. (b) Relative variation in the fracture energy of the phase-separated glass (G_c^{glass}) as a function of the reduced Young's modulus of the nanoinclusion particles (E^{part}/E^{mat}) for selected reduced fracture energy (G_c^{part}/G_c^{mat}).

C. Effect of the fracture energy of the nanoinclusions

We now assess the effect of a dissimilarity in fracture energy between the matrix and nanoinclusions. Fig. 4(a) shows the stress-strain curves of phase-separated glasses for selected fracture energy values for the nanoinclusions while keeping fixed their Young's modulus. As expected, we observe that, in this case, the elastic regime (i.e., before yield and fracture) remains unaffected by the presence of the nanoinclusions. However, we note that the ultimate strain (and ultimate stress) before fracture increases with increasing nanoinclusion fracture energy. This arises from that fact that an increase in the fracture energy of the nanoinclusions effectively increases the overall cohesion of the phase-separated glass and, thereby, increases the yield stress of the system. In addition, we note the appearance of plastic-like behavior (manifesting itself as a small plateau in the stress–strain curve before fracture) for high values of nanoinclusion fracture energy. This suggests that, in this regime, the phase-separated glass exhibits some strain hardening [51] and can be irreversibly deformed while keeping the stress constant.

Fig. 4(b) shows the evolution of the resulting fracture energy of the phase-separated glasses as a function of the fracture energy of the nanoinclusions (for selected nanoinclusion Young's moduli). We observe that, in this case, the fracture energy of the phase-separated glass monotonically increases with the fracture energy of the nanoinclusions, irrespectively of their stiffness (see also Fig. 3(b)). However, a break of slope is observed, namely, the fracture energy of the phase-separated increases faster when the nanoinclusions become tougher than the matrix and it decreases when the nanoinclusions become weaker (i.e., less tough) than the matrix. This can be understood from the fact that, when the nanoinclusions are weaker than the matrix, they do not carry any significant load once the glass is placed under tension, so that, in this regime,

the overall fracture energy of the phase-separated glass only weakly depends on the mechanical properties of the nanoinclusions.

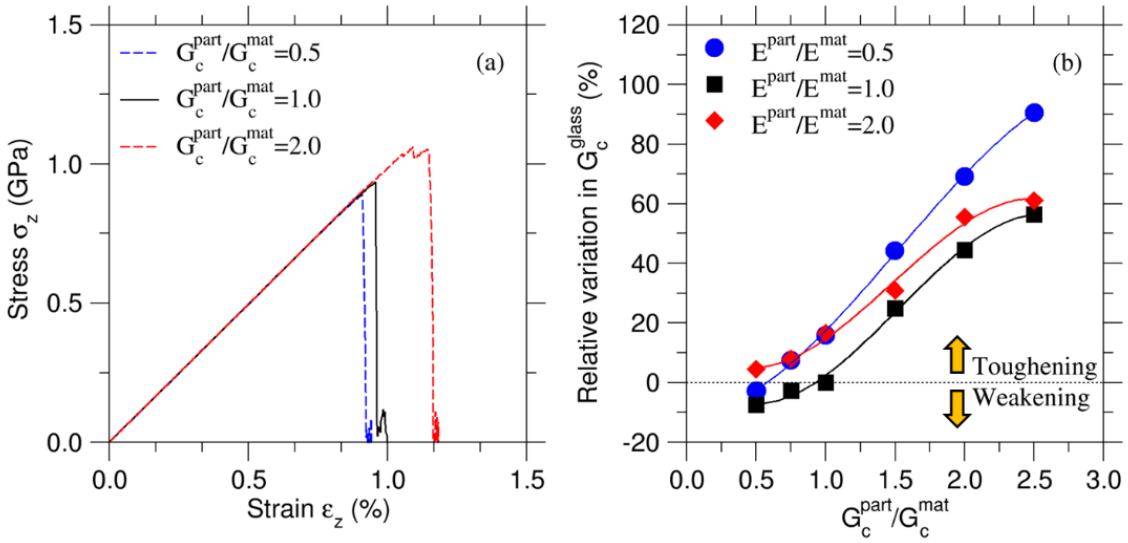

Figure 4. (a) Computed stress–strain curves for select values of fracture energy (G_c^{part}) for the nanoinclusion particles—the properties of the matrix (E^{mat}, G_c^{mat}) remaining constant and with $E^{part} = E^{mat}$. (b) Relative variation in the fracture energy of the phase-separated glass (G_c^{glass}) as a function of the reduced fracture energy of the nanoinclusion particles (G_c^{part}/G_c^{mat}) for selected reduced Young's moduli (E^{part}/E^{mat}).

Fig. 5 presents the combined effects on the overall fracture energy of the phase-separated glass of a dissymmetry between the Young's modulus and fracture energy of the matrix and nanoinclusions. Overall, we note that, at the exception of the case where the nanoinclusions have a lower fracture energy but the same stiffness as the matrix, the fracture toughness of the glass systematically increases upon the presence of phase separation. Based on these results, we find that the most significant increase in the fracture energy is achieved when the nanoinclusions

exhibit high fracture energy, but low stiffness (i.e., lower right corner of Fig. 5). The origin of this observation is discussed in Sec. 3.4.

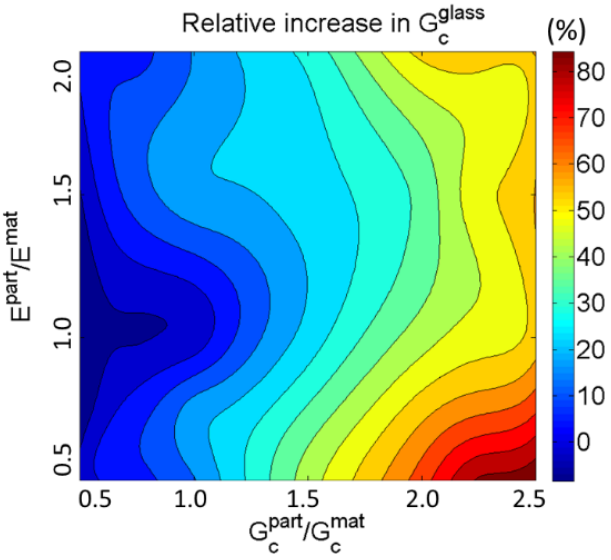

Figure 5. Contour plot summarizing the combined effects of the stiffness and toughness of the nanoinclusions on the overall fracture energy of the phase-separated glass.

D. Nature of the toughening mechanism

We now discuss the origin of the enhancement of fracture energy for each of the regimes previously mentioned (see Secs. 3.2 and 3.3). To this end, we analyze the different contributions to the fracture energy of the phase-separated glass (G_c^{glass}), as described in the following. We first decompose the fracture energy of the phase-eparated glass as:

$$G_c^{glass} = G^{coh} + G^{other} \tag{8}$$

where G^{coh} is the effective cohesive energy of the phase-separated glass (which accounts for the effective surface energy and real crack area) and G^{other} captures all other types of energy

contributions that are dissipated through plastic events (e.g., energy dissipated during crack deflection, crack pinning, crack trapping and bridging, etc. [19]). The effective cohesive energy of the phase-separated glass (G^{coh}) can be further expressed as:

$$G^{\text{coh}} = 2\gamma^{\text{glass}} \cdot k \tag{9}$$

where γ^{glass} is the effective surface energy of the phase-separated glass (as experienced by the crack during its propagation) and $k = A^{\text{glass}} / A_0$ is a geometrical factor that captures the fact that the real crack surface area A^{glass} is larger than the cross-section of the sample A_0. The geometry and area of the crack geometry are here extracted *post-mortem* by following the procedure provided in a previous work [52]. The effective surface energy of the phase-separated glass is then defined as:

$$\gamma^{\text{glass}} = (1-\varphi)\,\gamma^{\text{mat}} + \varphi\gamma^{\text{part}} \tag{10}$$

where γ^{mat} and γ^{part} are the surface energy of the matrix and nanoinclusion particles, respectively, and φ is the fraction of the final crack surface that crosses the nanoinclusions ($1-\varphi$ being the fraction of the crack surface that crosses the matrix). As such, the effective cohesive energy of the phase-separated glass (G^{coh}) captures the real overall cohesion energy that is experienced by the crack as it propagates. Note that this term differs from the average cohesion of the phase-separated glass as it depends on the propensity of the crack to be deflected either toward or around the nanoinclusions. Based on this formalism, one can define a brittleness index as:

$$B = \frac{G^{\text{coh}}}{G_c^{\text{glass}}} \tag{11}$$

wherein B = 1 corresponds to a perfectly brittle fracture, that is, where $G^{other} = 0$. In the following, we investigate to what extent each of these energy contributions contributes to increasing the fracture energy of the phase-separated glass.

We first investigate how the mechanical properties of the nanoinclusions control where the crack eventually propagates. Indeed, the existence of local stress heterogeneity can force the crack to propagate in the non-planar direction, which can result in some crack deflection. [26] Fig. 6(a) shows the fraction φ of the final crack surface that crosses the nanoinclusions (i.e., rather than the matrix) as a function of the Young's modulus of the nanoinclusions (for selected nanoinclusion fracture energy). Note that, in the absence of any crack deflection, one gets $\varphi \approx 30\%$ i.e., the volume fraction of the nanoinclusions. As such, $\varphi > 30\%$ indicates that the crack is attracted toward the nanoinclusions whereas $\varphi < 30\%$ indicates that the crack tends to go around the nanoinclusions (see the schematics in Fig. 6(a)). Overall, we observe that φ systematically increases with decreasing values of nanoinclusion fracture energy. As expected, this indicates that the crack preferentially propagates through the weak regions (i.e., low local fracture energy) and tend to avoid the tough regions. In addition, we observe that φ also increases with decreasing values of nanoinclusion stiffness (see Fig. 6(a)). This can be explained by that fact that the local stress intensity factor near the crack tip is affected by the local stiffness. According to Eshelby equivalent inclusion approach and finite element analysis, the mode I stress intensity factor increases with E^{part}/E^{mat} when the inclusion lies on the crack front [53]. As a result, the crack is more likely to deflect within the matrix with stiff inclusions. On the contrary, soft inclusions can effectively attract the crack. Moreover, the crack deflection is observed in the stiff nanoinclusion reinforced glass by recent molecular dynamics simulation [54]. Overall, we find that the propensity for crack deflection is controlled by a balance between the stiffness and

toughness of the nanoinclusions. We note that stiffness and toughness have a fairly similar influence on the propensity for crack deflection. Indeed, for instance, no propensity for crack deflection is observed in a phase-separated glass wherein the fracture energy and Young's modulus of the nanoinclusions are two times lower and larger than those of the matrix, respectively (see Fig. 6(a)). Crack deflection has multiple effects on the fracture energy of the phase separated glass by: (i) changing the effective surface energy experienced by the crack upon propagation (which is captured by γ^{glass}, see Eq. 10), (ii) affecting the roughness of the crack surface (i.e., its final surface, as captured by the coefficient $k = A^{\text{glass}} / A_0$ in Eq. 9), and (iii) resulting in plastic energy dissipation (as captured by G^{other}, see Eq. 8). Each of these energy contributions is described in the following.

We first focus on the effective surface energy experienced by the crack during propagation, which solely depends on the fraction φ of the final crack surface that crosses the nanoinclusions and the surface energies of each phase (see Eq. 10). As shown in Fig. 6(b), we observe that the effective surface energy of the phase-separated glass remains constant when the fracture energies (and, hence, surface energies) of the matrix and nanoinclusions are equal to each other. Indeed, in this case, the specific path of the crack is relevant. We then observe that the effective surface energy increases with increasing values of the nanoinclusion fracture energy. This is expected as an increase in the fracture energy (and, hence, surface energy) of the nanoinclusions increases the overall average cohesion of the phase-separated glass. However, we note that, at fixed high values of nanoinclusion fracture energy, the effective surface energy decreases with increasing values of nanoinclusion stiffness (see red series in Fig. 6(b)). This arises from the fact that the crack tends to avoid stiff particles (see Fig. 6(a)). In contrast, we note that, at fixed low values of nanoinclusion fracture energy, the effective surface energy increases with increasing values of

nanoinclusion stiffness (see blue series in Fig. 6(b)). Again, this arises from the fact that the crack tends to avoid stiff particles (see Fig. 6(a)), which, in this case, is beneficial as the nanoinclusions exhibit a lower toughness than the matrix. Altogether, we find that the effective surface energy experienced by the crack during propagation is controlled by a balance between the fracture energy of each phase and the propensity for the crack to avoid or go toward the nanoinclusions. Overall, these results show that an optimal increase in the effective surface energy of the phase-separated glass is achieved in the presence of soft, yet tough nanoinclusions—as such nanoinclusions favor the deflection of the crack toward the high-fracture-energy regions of the glass. In contrast, minimum effective surface energy is obtained in the presence of soft and weak nanoinclusions—as such nanoinclusions favor the deflection of the crack toward the low-fracture-energy regions of the glass.

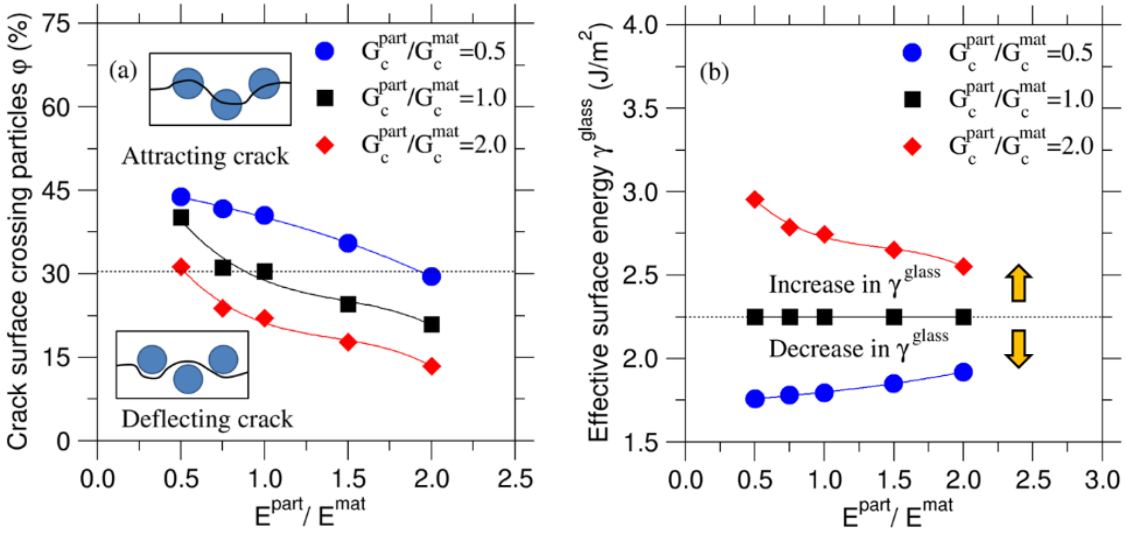

Figure 6. (a) Fraction of the final crack surface that crosses the nanoinclusions as a function of the reduced Young's modulus of the nanoinclusion particles (E^{part}/E^{mat}) for selected reduced fracture energy (G_c^{part}/G_c^{mat}). The dotted line indicates the average surface fraction covered by particles (about 30%), that is, the fraction of the crack surface

crossing the particles if no deflections are observed. (b) Effective surface energy (γ^{glass}, see Eq. (10)) experienced by crack during propagation in the phase-separated glass as a function of the reduced Young's modulus of the nanoinclusion particles (E^{part}/E^{mat}) for selected reduced fracture energy (G_c^{part}/G_c^{mat}). The dotted line indicates the surface energy of the matrix, that is, in the absence of any phase separation.

We now investigate the energy contribution of the roughness of the final crack surface that results from the presence of some crack deflection. Such rough crack surface have been observed in nanoparticle-reinforced epoxy nanocomposites [56,57]. Fig. 7(a) shows the area of the final crack surface A^{glass}, normalized by the cross-section of the sample A_0 (i.e., a metric that captures the roughness of the crack surface). Overall, we observe that, at the exception of the case where the glass is fully homogeneous (i.e., with no phase separation), the real area of the crack surface is systematically larger than the cross-section of the sample. This is expected as the cross-section represents the minimum theoretical value of the crack surface, i.e., the shortest path from the crack to reach the right end of the sample. We observe that the area of the crack surface increases with increasing dissimilarity in the mechanical properties of the matrix and nanoinclusions, that is, when the crack has a propensity to avoid or be attracted by the nanoinclusions (see Fig. 6(a)). Overall, we find that the maximum increase in the roughness of the crack is achieved in the presence of tough and stiff nanoinclusions (see Fig. 7(a)), that is, when the crack presents the highest propensity to avoid the nanoinclusions (see Fig. 6(a)). Experimental observations also support these conclusions—as scanning electron microscopy (SEM) micrographs obtained on fractured nano-particle-modified epoxy phases suggest that particle debonding/pullout is the main mode of fracture in the presence of nano-silica particles (i.e., stiff inclusions), whereas nanocavitation is observed in the presence of rubber particles (i.e., soft inclusions) [55].

However, we note that, in all cases, the increase in the crack surface remains limited (7.5% at most for the range of parameters explored herein). This suggests that the geometrical roughness of the crack surface has a low contribution to the overall cohesion of the phase-separated glasses. Indeed, as shown in Fig. 7(b) , the effective cohesive energy of the phase-separated glass (G^{other} , see Eq. 9) closely follows the value of the effective surface energy (γ^{glass} , with a factor of 2, see Eq. 9). Crack roughness only results in a small increase in the effective cohesion energy of the glass in the case of tough and stiff nanoinclusions.

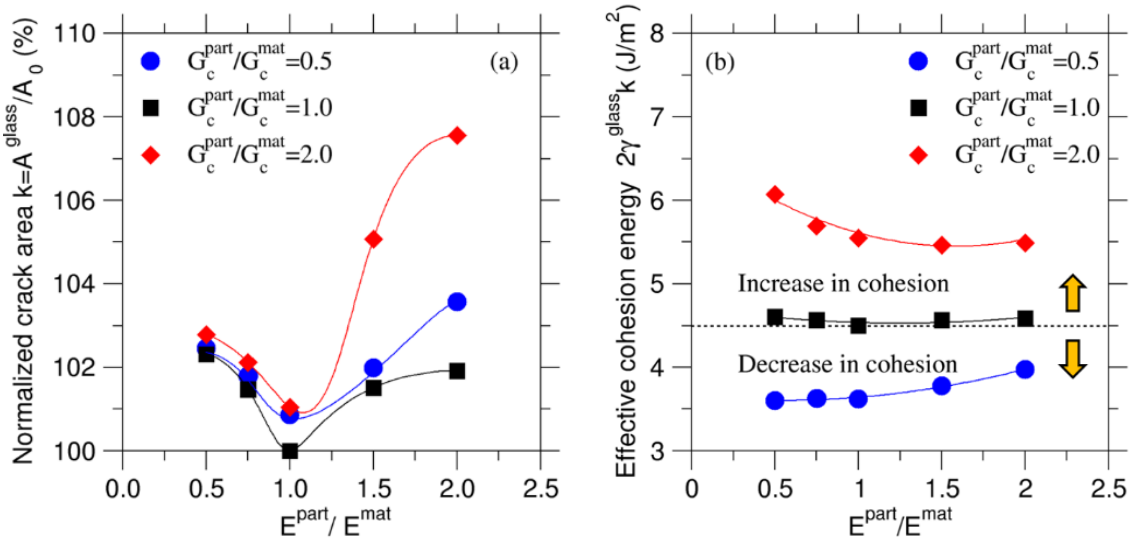

Figure 7. (a) Area of the final crack (normalized by the cross-section of the sample) as a function of the reduced Young's modulus of the nanoinclusion particles ($E^{\text{part}}/E^{\text{mat}}$) for selected reduced fracture energy ($G_c^{\text{part}}/G_c^{\text{mat}}$). (b) Effective cohesion energy (see Eq. (9)) of the phase-separated glass. The dotted line indicates the cohesion energy of the matrix, that is, in the absence of any phase separation.

Finally, we investigate the energy contribution that is dissipated through some plastic events. Fig. 8(a) shows the plastic component of the fracture energy of the phase-separated glasses (G^{other}), which is calculated by subtracting the effective cohesive energy from the total fracture energy (see Eq. 8). We observe that the dissipated energy increases with higher degree of dissymmetry between the mechanical properties of the matrix and nanoinclusions. We observe that the amount of dissipated energy is significantly higher in the case of tough nanoinclusions than for weak nanoinclusions. Overall, the dissipated energy exhibits a trend that is fairly similar to that of the area of the crack surface (see Fig. 7(a)). This suggests that such dissipated energy primarily arises from some variations in the direction of the crack propagation. In the case of stiff nanoinclusions, the dissipated energy is expected to mostly arise from crack deflections [26]. In the case of soft nanoinclusions, the dissipated energy is expected to mostly arise from crack trapping and bridging [28]. In both cases, phase separation results in a significant decrease in the degree of brittle fracture (see Fig. 8(b)).

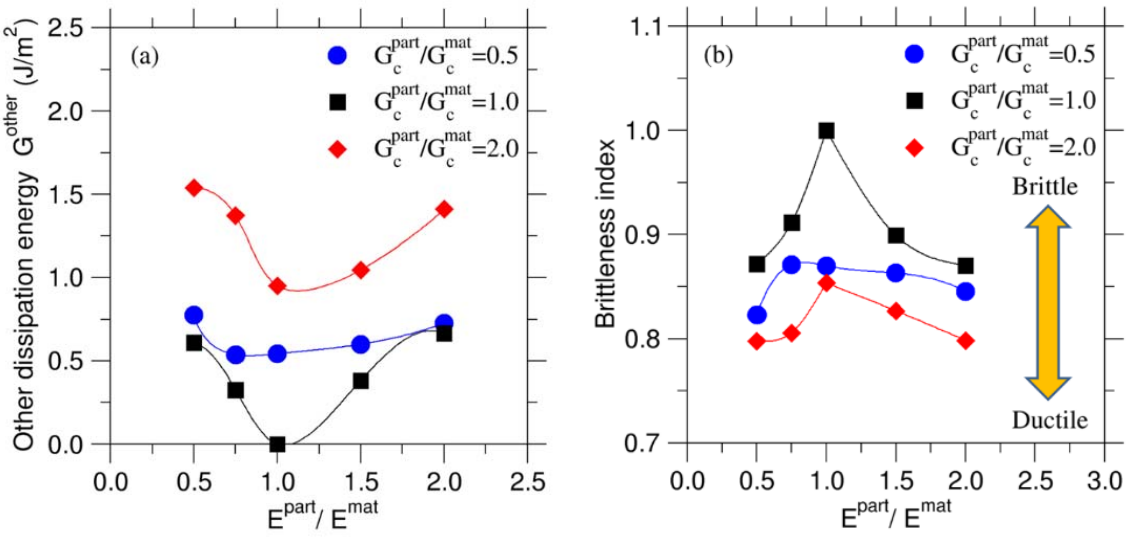

Figure 8. (a) Energy dissipated through ductile events and (b) brittleness index (see Eq. (11)) as a function of the Young's modulus of the particles (E^{part}) for selected particle fracture energy (G_c^{part}), wherein the particles' mechanical properties are normalized by those of the matrix (E^{mat} and G_c^{mat}).

IV. DISCUSSION

Altogether, these results allow us to identify the underlying toughening mechanism for each type of system (see Fig. 5). We note that the presence of phase separation systematically results in an increase in the fracture toughness of the glass, with the exception of the case of weak and soft nanoinclusions (see Fig. 3(b) and Fig. 4(b)). In this situation, the low stiffness of the nanoinclusions tend to attract the crack (see Fig. 6(a)) toward the weak nanoinclusions, which results in a decrease in the effective cohesion of the phase-separated glass (see Fig. 6(b)). In contrast, all the other situations cause the fracture energy to increase. First, in the case of weak and stiff nanoinclusions, some crack deflection is observed (see Fig. 6(a)). Although this results in a decrease in the cohesion of the glass (see Fig. 6(b)), this loss of energy is counter-balanced by the existence of some plastic dissipated energy arising from the crack deflection mechanism

(see Fig. 8(a)). Second, in the case of tough and stiff nanoinclusions, a significant degree of crack deflection is observed, wherein the crack shows a high propensity to avoid the nanoinclusions (see Figs. 6A and 7A). Although the increase in the effective cohesion of the glass is limited (see Fig. 6(b)), the crack deflection mechanism is associated with a large amount of plastic energy dissipation (see Fig. 8(a)). Finally, the largest extent of toughening is achieved in the case of tough and soft nanoinclusions. In this situation, the low stiffness of the nanoinclusions tend to attract the crack (see Fig. 6(a)) toward the tough nanoinclusions, which results in a large increase in the effective cohesion of the phase-separated glass (see Fig. 6(b)). This is augmented by a large amount of plastic energy dissipation (see Fig. 8(a)). Overall, our results suggest that the presence of soft, yet tough nanoinclusions is the most promising route toward the development of tougher phase-separated glasses that retain their transparency.

In practice, depending on the composition of the glass and its position with respect to the immiscibility dome, the phase separation of calcium silicate glasses can result in the formation of Ca- or Si-rich nanoinclusions [35]. In the first case, the Ca-rich droplets are likely to be stiffer, but weaker than the matrix [48,58]. Our results suggest that this situation would result in only a minor increase in the fracture toughness of the phase-separated glass. However, in the second case, the Si-rich droplets are likely to be softer, but tougher than the matrix [48,58]. Based on previous molecular dynamics simulations, this situation would yield $E^{part}/E^{mat} = 0.7$ and $G_c^{part}/G_c^{mat} = 2.1$ [48]. Based on the present study, one can, therefore, expect the phase-separated glass would exhibit a 60% increase in its fracture energy with respect to that of the isochemical homogeneous glass (see Fig. 5).

Note that these predictions are restricted to microstructures consisting in small spherical droplets. On the one hand, it is likely that the magnitude of the toughening effects identified herein would

increase in the presence of larger inclusions. On the other hand, spinodal decomposition (which occurs when the glass composition is located in the middle of the immiscibility domain) would result in the formation of rather large interconnected phases. The propensity for this kind of microstructure is likely to be superior to that of matrix–droplets microstructures, so that the increase in toughness resulting from spinodal decomposition is likely to be higher than that induced by nucleation-growth [15]. However, this kind of microstructure typically result in a loss of transparency, which reduces the range of potential applications for such phase-separated glasses.

V. Conclusion

Overall, our peridynamics simulations offer a realistic description of the effect of nanoscale phase separation on the fracture behavior of silicate glasses. We show that, in most cases, phase separation results in an increase in the fracture energy of the glass. By quantifying the various contributions to the fracture energy, we show that the extent of toughening is governed by a balance between the propensity for crack deflections, the effective cohesion of the phase-separated glass, the existence of plastic energy dissipation, and (to a lower extent) the roughness of the crack surface. The largest extent of toughening is achieved in the case of soft, yet tough nanoinclusions. In this situation, the crack shows a high propensity for traveling through the softer nanoinclusions, which results in a large increase in the effective cohesion of the phase-separated glass. In all cases, phase separation results in some significant plastic energy dissipation, which renders it a promising route toward the development of novel phase-separated glasses that exhibit some nanoductility while retaining their optical transparency.

Acknowledgements

The authors acknowledge financial support provided by the National Science Foundation under Grant No. 1762292, the National Key R&D Program of China under Grant No. 2016YFC0401907, the National Natural Science Foundation of China under Grant No. 5157090787, and the International Graduate Student Exchange Program of Wuhan University.

References

[1] J. C. Mauro and E. D. Zanotto, Int. J. Appl. Glass Sci. **5**, 313 (2014).
[2] J. C. Mauro, Fontiers Mater. **1**, 20 (2014).
[3] L. Wondraczek, J. C. Mauro, J. Eckert, U. Kühn, J. Horbach, J. Deubener, and T. Rouxel, Adv. Mater. **23**, 4578 (2011).
[4] Y. Shi, J. Luo, F. Yuan, and L. Huang, J. Appl. Phys. **115**, 043528 (2014).
[5] Rouxel Tanguy and Yoshida Satoshi, J. Am. Ceram. Soc. **100**, 4374 (2017).
[6] J. J. Lewandowski, M. Shazly, and A. Shamimi Nouri, Scr. Mater. **54**, 337 (2006).
[7] R. O. Ritchie, Nat. Mater. **10**, 817 (2011).
[8] R. Briard, C. Heitz, and E. Barthel, J. Non-Cryst. Solids **351**, 323 (2005).
[9] A. R. Boccaccini and V. Winkler, Compos. Part Appl. Sci. Manuf. **33**, 125 (2002).
[10] M. Bauchy, B. Wang, M. Wang, Y. Yu, M. J. Abdolhosseini Qomi, M. M. Smedskjaer, C. Bichara, F.-J. Ulm, and R. Pellenq, Acta Mater. **121**, 234 (2016).
[11] K. Januchta, R. E. Youngman, A. Goel, M. Bauchy, S. L. Logunov, S. J. Rzoska, M. Bockowski, L. R. Jensen, and M. M. Smedskjaer, Chem. Mater. **29**, 5865 (2017).
[12] P. F. James, J. Mater. Sci. **10**, 1802 (1975).
[13] N. Kreidl, J. Non-Cryst. Solids **129**, 1 (1991).
[14] A. K. Seal, P. Chakraborti, N. R. Roy, S. Mukherjee, M. K. Mitra, and G. C. Das, Bull. Mater. Sci. **28**, 457 (2005).
[15] N. Soga, J. Non-Cryst. Solids **73**, 305 (1985).
[16] N. Miyata and H. Jinno, J. Non-Cryst. Solids **38**–**39**, 391 (1980).
[17] S. Cheng, C. Song, and P. Ercius, Phys. Chem. Glas. - Eur. J. Glass Sci. Technol. Part B (2017).
[18] A. K. Varshneya, *Fundamentals of Inorganic Glasses* (Academic Press Inc, 1993).
[19] B. C. Kim, S. W. Park, and D. G. Lee, Compos. Struct. **86**, 69 (2008).
[20] P. Rosso, L. Ye, K. Friedrich, and S. Sprenger, J. Appl. Polym. Sci. **100**, 1849 (2006).
[21] G. Hantal, L. Brochard, R. J.-M. Pellenq, F.-J. Ulm, and B. Coasne, Langmuir (2017).
[22] K. C. Jajam and H. V. Tippur, Int. J. Solids Struct. **49**, 1127 (2012).
[23] D. Quesada, D. Leguillon, and C. Putot, Eur. J. Mech. - ASolids **28**, 668 (2009).
[24] L.-C. Tang, X. Wang, Y.-J. Wan, L.-B. Wu, J.-X. Jiang, and G.-Q. Lai, Mater. Chem. Phys. **141**, 333 (2013).
[25] A. R. Boccaccini and P. A. Trusty, J. Mater. Sci. Lett. **15**, 60 (n.d.).

[26] K. T. Faber and A. G. Evans, Acta Metall. **31**, 565 (1983).
[27] M. Y. He, A. G. Evans, and J. W. Hutchinson, Int. J. Solids Struct. **31**, 3443 (1994).
[28] A. F. Bower and M. Ortiz, J. Mech. Phys. Solids **39**, 815 (1991).
[29] H. Gao and J. R. Rice, J. Appl. Mech. **56**, 828 (1989).
[30] M. Kotoul and J. Vrbka, Theor. Appl. Fract. Mech. **40**, 23 (2003).
[31] F. F. Lange, Philos. Mag. J. Theor. Exp. Appl. Phys. **22**, 0983 (1970).
[32] B. Budiansky, J. C. Amazigo, and A. G. Evans, J. Mech. Phys. Solids **36**, 167 (1988).
[33] G. Bao and Z. Suo, Appl. Mech. Rev. **45**, 355 (1992).
[34] G. H. Beall and L. R. Pinckney, J. Am. Ceram. Soc. **82**, 5 (1999).
[35] L. Martel, M. Allix, F. Millot, V. Sarou-Kanian, E. Véron, S. Ory, D. Massiot, and M. Deschamps, J. Phys. Chem. C **115**, 18935 (2011).
[36] S. A. Silling, J. Mech. Phys. Solids **48**, 175 (2000).
[37] S. A. Silling and E. Askari, Comput. Struct. **83**, 1526 (2005).
[38] S. A. Silling and R. B. Lehoucq, in *Adv. Appl. Mech.*, edited by H. Aref and E. van der Giessen (Elsevier, 2010), pp. 73–168.
[39] O. C. Zienkiewicz, *The Finite Element Method*, 3d expanded and rev. ed (McGraw-Hill, London□; New York, 1977).
[40] O. C. Zienkiewicz, R. L. Taylor, and R. L. Taylor, *The Finite Element Method: Solid Mechanics* (Butterworth-Heinemann, 2000).
[41] S. A. Silling, M. Epton, O. Weckner, J. Xu, and E. Askari, J. Elast. **88**, 151 (2007).
[42] E. Madenci and E. Oterkus, *Peridynamic Theory and Its Applications* (Springer New York, New York, NY, 2014).
[43] J. G. M. Van Mier and M. R. A. Van Vliet, Eng. Fract. Mech. **70**, 2281 (2003).
[44] O. Yılmaz and J.-F. Molinari, Cem. Concr. Res. **97**, 84 (2017).
[45] X. Wang, M. Zhang, and A. P. Jivkov, Int. J. Solids Struct. **80**, 310 (2016).
[46] A. Yaghoobi, M. G. Chorzepa, S. S. Kim, and S. A., Materials **10**, 162 (2017).
[47] A. Agwai, I. Guven, and E. Madenci, Int. J. Fract. **171**, 65 (2011).
[48] B. Wang, Y. Yu, Y. J. Lee, and M. Bauchy, Front. Mater. **2**, (2015).
[49] M. L. Parks, D. J. Littlewood, J. A. Mitchell, and S. A. Silling, *Peridigm Users' Guide. V1.0.0.* (2012).
[50] F. Bobaru and G. Zhang, Int. J. Fract. **196**, 59 (2015).
[51] J. R. Rice and G. F. Rosengren, J. Mech. Phys. Solids **16**, 1 (1968).
[52] M. Bußler, P. Diehl, D. Pflüger, S. Frey, F. Sadlo, T. Ertl, and M. A. Schweitzer, Comput. Graph. **67**, 45 (2017).
[53] Z. Li and Q. Chen, Int. J. Fract. **118**, 29 (2002).
[54] S. Urata, R. Ando, M. Ono, and Y. Hayashi, J. Am. Ceram. Soc. **101**, 2266 (n.d.).
[55] L.-C. Tang, H. Zhang, S. Sprenger, L. Ye, and Z. Zhang, Compos. Sci. Technol. **72**, 558 (2012).
[56] B. B. Johnsen, A. J. Kinloch, R. D. Mohammed, A. C. Taylor, and S. Sprenger, Polymer **48**, 530 (2007).
[57] H. Zhang, Z. Zhang, K. Friedrich, and C. Eger, Acta Mater. **54**, 1833 (2006).
[58] R. J. Eagan and J. C. Swearekgen, J. Am. Ceram. Soc. **61**, 27 (1978).